



Full Length Article

Facile fabrication of flexible Si-based nanocomposite films as high-rate anodes by layer-by-layer self-assembly



Lehao Liu^{a,b}, Meicheng Li^{a,*}, Lihua Chu^a, Bing Jiang^a, Ruoxu Lin^b

^a State Key Laboratory of Alternate Electrical Power System with Renewable Energy Sources, North China Electric Power University, Beijing 102206, China

^b Citic Guoan MGL Power Source Technology Company Limited, Beijing 102200, China

ARTICLE INFO

Keywords:

Copper nanoparticle
Silicon particle
Flexible nanocomposite film
Battery anode

ABSTRACT

Silicon is a promising anode material for high-performance Li-ion batteries, but the high capacity of silicon is mainly restrained by its large volume change upon electrochemical cycling. Herein, flexible nanocomposite films of polyurethane/copper/silicon were facilely fabricated by an improved layer-by-layer self-assembly method. This method can not only avoid the particle agglomeration in the nanocomposites, but also effectively combine the typical property advantages of the three building blocks—Li storage capability of silicon, electro-conductivity of copper, and stretchability of polyurethane. The self-organization of the copper nanoparticles into necklace-like chains and three-dimensionally conductive networks during the preparation process furtherly facilitated the electron transfer in the composite films. The multifunctional films had improved mechanical flexibility (8.2 MPa tensile strength with 125.1% strain) and electro-conductivity (8 S cm^{-1}), and can be directly used as anodes for accommodating the silicon volumetric change and preserving the electrical contact upon electrochemical cycle. Thus, the nanocomposite film electrodes showed high capacity of 574 mAh g^{-1} after 300 cycles at 1 C and average Coulombic efficiencies of 99.2–99.8%. This work offers an simple and effective material design way to fabricating multifunctional composite films with single-function building units for energy storage applications.

1. Introduction

Owing to its obvious advantages of higher theoretic capacity of $4200 \text{ (Li}_{22}\text{Si}_5)$ or $3580 \text{ mAh g}^{-1} \text{ (Li}_{15}\text{Si}_4)$ [1], higher safety, better environmental friendliness and abundance than graphite materials (372 mAh g^{-1} , LiC_6) [2], silicon (Si) has been studied as an anode material replacement for graphite to meet high-performance Li-ion battery (LIB) applications [3]. Nevertheless, the practical implementation of Si is still hindered dramatically by its sluggish cycle performance (Fig. 1A) [4], which is mainly caused by serious pulverization of the anode and the continuous generation of solid electrolyte interphase (SEI) and poor electric connection with current collector resulted from the Si volume change of 300–400% upon full lithiation/delithiation [5].

Decreasing the particle size to nanoscale level (e.g., nanoparticles (NPs) [6], nanowires [7], and nanotubes [8]) can effectively relieve the internal stress/strain induced by the large Si expansion/shrink upon lithiation/delithiation for greatly-improved cycling stability. Nevertheless, the huge surface area of the Si nanomaterials also results in low tap density, agglomeration, side reactions, much more SEI formation, thermal runaway, etc., which are detrimental to their commercial applications [9].

To circumvent these new obstacles, anchored, core-shelled, porous and flexible structures have been designed by compositing the Si-based nanomaterials with other matrix materials [9]. The Si nanoparticles anchored on the electrical matrices can relieve the Si volumetric change during lithiation/delithiation, prevent the Si nanoparticle aggregation, and promote the electron transfer; however, the anchored Si materials would incline to fall off from the supporting substrates under high-current cycling [10]. Because of the less structural stress and damage and better electronic conductivity than Si during cycling, carbon is usually chosen to make core-shelled structures with Si [11]. The hollow Si-carbon core-shell structures would better allow Si to expand/shrink without destroying the shell and thereby improve the cycling stability [12]. Nevertheless, the preparation of the core-shelled or yolk-shelled particles needs intricate processes including the carbonization of polymers at high temperature and the removal of silica from the Si surface by hydrofluoric acid [12–14]. Making hollow or porous Si particles can also tolerate the large volume variation by the abundant voids, but the acid etch process is usually used in the preparation procedure [15]. Besides, making Si-based porous electrodes by depositing Si on porous copper (Cu), nickel, or carbon matrices would also effectively relieve the Si volumetric change and promote the electron

* Corresponding author.

E-mail address: mcli@ncepu.edu.cn (M. Li).

<https://doi.org/10.1016/j.apsusc.2019.01.075>

Received 8 October 2018; Received in revised form 17 December 2018; Accepted 8 January 2019

Available online 09 January 2019

0169-4332/ © 2019 Elsevier B.V. All rights reserved.

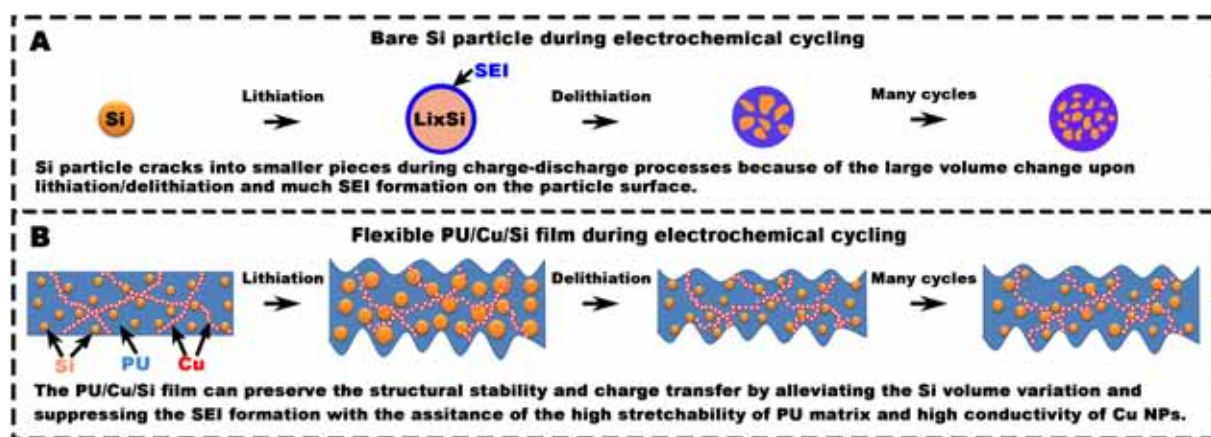


Fig. 1. Schematic illustration of the structure/morphology changes of (A) bare Si particles and (B) LBL-resulted flexible composite film anode during charge-discharge.

transfer for better cycling performance [16,17]. This electrode configuration is binder/conductive additive-free [18]. But the complexity of the porous electrode fabrication impedes their potential applications in commercial LIBs [18–20].

Fortunately, flexible composite film anode structures can be fabricated by combining the Si-based nanomaterials with electro-conductive and flexible matrix materials (e.g., carbon nanotubes and graphene) [21–23]. The high conductivity of the matrices can promote the electron transfer, while the high flexibility is conducive to relieving the Si volume variation-induced stress/strain [21,23,24]. The total weight of the flexible composite anode-based batteries is also decreased, due to the removal of the copper current collectors [9,25]. Nevertheless, it is difficult to obtain a uniform distribution of the nanoparticles in the composite films by the simple physical mixing, because of the agglomeration of the nanoparticles [9,26]. Thus, simple and effective methods for preparing flexible Si-based composite films are still desired.

Layer-by-layer (LBL) self-assembly has been thought to be an exceptionally reliable engineering method for making various composite films [27,28] with simpler combination of multiple properties, because of the obvious advantages of nanometer-level regulation of the composite materials, conformal coverage of complex geometries, effective inhibition of the phase separation of particle solution (or aggregation of particles), etc [29,30]. Polyurethane (PU)/gold (Au) composite films have been developed by LBL self-assembly of negatively-charged Au and positively-charged PU, and the films showed ultrahigh flexibility and conductivity due to the effective integration of the high-stretchability PU and high-conductivity Au NP [31].

PU contains both hard and soft sections, and these two phases connect each other in the whole system. The hard parts in PU offer spatial stability and mechanical strength, while the soft parts are conducive to good ionic conductivity because the soft segments do not form ionic clusters after being dissolved in alkali metals [32–35]. Li^+ ions would coordinate with the oxygen and nitrogen-based groups in the soft parts (Fig. S1A–B) [33,35], and the segmental motion of the polymer chains results in the ionic conductivity. Because of the effective combination of high mechanical toughness, thermal stability, ionic conductivity, wide electrochemical window and wettability of liquid organic electrolytes, PU is widely used as polymer matrices of gel polymer [32,36,37] and solid polymer [33–35,38,39] electrolytes, binders [40], and separators [40–42] in LIBs.

Herein, flexible Si-based nanocomposite films were prepared by LBL self-assembly with the assistance of the strong electrostatic attractions between the electronegative silicon and copper nanoparticles and electropositive polyurethane (Fig. 1B). This method was simple and effective for fabricating the flexible composite films without the particle

agglomeration. Because of the effective property integration of the Li storage capability of silicon, electro-conductivity of copper and mechanical stretchability of polyurethane, the resulted composite films also displayed excellent electrical and mechanical properties. The self-assembly of the copper particles into necklace-like chains and three-dimensionally (3D) conductive metal networks in the films further promoted the electron transfer. The anode films can keep the structural stability and efficient charge transport during the charge-discharge (C–D) processes by effectively relieving the silicon volume variation and inhibiting the SEI formation, and thus exhibited greatly-enhanced cycling performance.

2. Experimental section

2.1. Preparation of nanoparticle-based solutions and nanocomposite films

For synthesizing copper nanoparticle solution without severe copper oxidation, the synthesis method reported by Wang and Asefa [43] was modified without the use of the NaOH and polyallylamine. 160 mg mercaptosuccinic acid (MSA) and 80 mg CuSO_4 were firstly stirred in 50 mL pure water and heated at 60 °C for 0.5 h under violent stirring. 5 mL N_2H_4 was subsequently dropped into the mixed solution for 0.5 h. After that the mixture solution was heated for 2–4 h. The obtained Cu NP solution was centrifuged at a high speed of 6,000 rpm for 0.5 h, and then redispersed with pure water by sonication for obtaining high-dispersity copper solution.

For well-dispersed silicon solution, silicon powders (0.5 mg/mL) were firstly sonicated in 10 mM Trizma-HCl buffering solution with a pH value of 8.0, centrifuged at 10,000 rpm for 0.5 h, and finally redispersed in pure water by strong sonication.

For the Si-based nanocomposites, glass slides were firstly pretreated in a piranha solution with $\text{H}_2\text{O}_2/\text{H}_2\text{SO}_4$ volume ratio of 1:3 for 12 h before use. This pretreatment can not only clean the glass slides but also promote the formation of hydroxyl groups on the glass substrates, which is helpful for the following self-assembly process with the assistance of the electrostatic attraction and hydrogen bonding interactions [44,45]. The clean substrate was firstly put in polyurethane solution with 1.0% concentration for 0.2 h, washed by pure water and desiccated by dry gas flow. The resulted glass substrate was then put in a mixture solution containing 1.5 mg mL^{-1} copper and 0.5 mg mL^{-1} silicon particles for 0.5 h, washed by pure water, and again desiccated by dry gas flow. The $(\text{PU}/\text{Cu}-\text{Si})_m$ nanocomposite films can be obtained by repeating these processes for m times. The sample was again put in polyurethane solution for 0.2 h, washed by pure water and desiccated by dry gas flow, and then treated with the copper solution (2 mg mL^{-1}) for 0.5 h, giving a (PU/Cu) bilayer. The desired composite films of

$[(\text{PU}/\text{Cu}-\text{Si})_m(\text{PU}/\text{Cu})]_N$ can be obtained by repeating the above-mentioned process for N times. Various composite films were also achieved by changing the assembly sequence and solution type. The nanocomposites can also be fabricated on the piranha solution-treated Cu foils. Through the acid pretreatment process, the color of the Cu substrates became more shining, and electro-conductivity increased to 3.0×10^5 from 2.3×10^5 S cm^{-1} . Because of the large specific surface areas of the NPs and the agglomeration behavior, the NP solutions were changed with fresh ones after tens of self-assembly cycles. HF aqueous solution was used to treat the substrates for free-standing composite films. The films were then cleaned with pure water and desiccated in a vacuum oven at 60 °C for at least 24 h before different measurements.

2.2. Characterizations and measurements

The morphological and structural characteristics of the nanoparticles and the nanocomposite films were observed by FEI Nova 200 or Hitachi SU8010 scanning electron microscope (SEM) and JEOL 3011 transmission electron microscope (TEM). A Malvern Zetasizer device was used to detect the particle size and zeta potential. Thermo gravimetric analysis (TGA) curves of the films were obtained in Ar atmosphere with a heating speed of 10 °C min^{-1} . Auger Nanoprobe (Model: PHI 680) was utilized to determine the elemental composition contents of the nanocomposite films. The voltage and current of the beam were 10 kV and 10 nA, respectively. Electric resistance of the films was achieved by an Agilent 34401A multimeter based on the commonly-used four-point-probe technology. A TestResources 100Q1000 device was applied to measure the mechanical tensile properties with 0.2 mm s^{-1} lifting speed. The force was divided by the initial width and thickness of the films for obtaining the stress. An Agilent 8453 UV–vis Chem spectrophotometer was used to get the absorbance spectra of the particles and the films.

For the electrochemical measurements, coin-type half-cells were assembled using Celgard polymer separators and 1 M LiPF_6 EC/DMC electrolyte. A nanocomposite film and a Li foil were directly utilized as working and counter electrode, respectively. The sandwich-structured half-cells were fabricated under argon protection with both the oxygen and moisture contents of < 0.1 ppm. The electrochemical cycling was operated by a Maccor 4000 48-channel battery device within 0.01–2.0 V at 0.1–2 C (1 C corresponded to 4 A g^{-1}). A CHI660D electrochemical workstation was applied to achieve the electrochemical impedance spectra (EIS) within a frequency range of 100k–0.01 Hz.

3. Results & discussion

3.1. Nanoparticle-based aqueous solutions

A chemical reduction method was developed to synthesize Cu NPs in pure water for following LBL self-assembled films. The Cu NPs with the reaction time of 2 h were in the form of necklace-like chain structure with an average diameter of 11.16 nm (Fig. 2A). The Cu NPs showed a lattice spacing of 0.21 nm (Fig. 2B), corresponded to the (1 1 1) interplanar distance of the face-centered cubic copper crystal. When increasing the reaction time to 4 h, the NPs almost kept the same size (11.24 nm) and chain shape (Fig. 2C and D), which would enable high electro-conductivity of the NP-based films. The desiccated NPs had a flocculent morphology (Fig. 2E), ascribed to the formation of the chain shape with the interconnected NPs (Fig. 2F). Previous studies have proven the unavoidable oxidation behavior of Cu NPs in the presence of air or water [46,47]. The EDS also showed the partial oxidation of the as-synthesized Cu NPs with oxygen content of ~3.06 wt% (Fig. 2H). The Cu NPs also displayed typical absorption peaks at 500–600 nm in the UV–vis absorbance spectra, and the red shift and broadening of the peaks also suggested the existence of the particle self-organization (Fig. 2G) [46,48,49].

We also prepared Si particle-based aqueous dispersion by sonicating

the Si particles in tris-HCl solution (Fig. 3A). Electron micrographs (Fig. 3B–D) showed the laser plasma-synthesized Si powders were mostly sphere and had a mean size of 123.0 ± 70.2 nm. The Si nanoparticles also showed a lattice space of 0.31 nm, agreeing well with the (1 1 1) interplanar distance of the Si crystal (Fig. 3E). The XRD pattern furtherly proven the high purity of the as-synthesized Si particles (Fig. 3F).

3.2. The nanoparticle-based composite films

To prepare flexible and conductive composite films, we used an improved LBL self-assembly method with the effective combination of the high-capacity Si particles, high-conductivity Cu NPs and high-stretchability PU (Fig. 4). The nanoparticle-based composite films were successfully assembled by alternative electrostatic adsorption of PU and Si and Cu particles, based on their opposite surface charge attractions (The corresponding zeta potentials were 49, –52 and –47 mV, Fig. S2). The necklace-like chained Cu NPs form a 3D conductive skeleton with the Si particles trapped in the nanocomposite films. This 3D conductive Cu network would promote the transfer of electrons, while the flexible PU frame can tolerate the Si volumetric expansion/shrink during the charge-discharge process for high battery performance (Fig. 1B).

In this study, the preparation of PU/Cu nanocomposite film was a vital step. The UV–vis absorbance spectrometry was used to disclose the LBL self-assembly process (Fig. 5A). We saw an obvious increase in absorbance with increasing bilayer numbers (N) due to the highly opposite charges of the PU and Cu NPs and strong electrostatic attractions between them. The inset plots depicting the absorbance at 365 nm versus the bilayer numbers clearly displayed a stepwise formation of the multilayer films. The vigorous growth of the films on the substrates was furtherly observed by the optical photography (Fig. 5B). The films also had a high Cu content of 79.7 wt% (Fig. 5C). SEM images (Fig. 5D–G) were taken to further investigate the microstructure of the free-standing composite films after the acid treatment. Due to the good electrical conductivity, no carbon or gold was sputtered on the films for SEM characterizations. The 140 bilayer composite film was ~3.4 μm in thickness (Fig. 5F) with a coarse top surface (Fig. 5D). The interconnected Cu NPs in the film still kept the chain structure, forming a 3D conductive metal network (Fig. 5E) that originated from the as-synthesized chained NPs (Fig. 2A–F). Even at the cracked lateral section the Cu particles still firmly linked together (Fig. 5G). Though the severe destruction of the nanocomposite structure by sonication treatment in ethanol, the chained Cu NPs still closely connected each other to form the 3D networks (Fig. 5H–I) and PU completely covered the Cu NPs (Fig. 5J). Such morphology should be conducive to metallic charge transport in the films.

The UV–vis absorbance spectrometry was further utilized for observing the assembly process of Si NPs and PU for nanocomposites on the glass substrates (Fig. 6A). Comparing to the spectra of PU and Si (Fig. S2D), we saw an obvious increase in absorbance in the PU/Si film spectra with the increasing bilayer number. The inset plots depicting the absorbance at 365 nm versus the bilayer numbers further verified the stepwise formation of the multilayer films. Optical photographs indicated that the yellow nanocomposite films with various bilayer number grew on the glass slides (Fig. 6B). The weight ratio of Si in the nanocomposite film was detected to be 69.5% (Fig. 6C). The (PU/Si)₅₀ film had a much coarser surface than the PU/Cu film (Fig. 6D) because of the wide size distribution of the Si particles (Fig. 3B–D). Moreover, the Si particles interconnected to each other with the assistance of PU (Fig. 6E), because of their strong electrostatic attractions. The thickness of the 50 bilayer nanocomposite was determined to be ~1.2 μm (Fig. 6F). TEM images furtherly showed that the Si particles were entirely encapsulated by the cationic PU layers (Fig. 6G–I), even after the vigorous sonication treatment in ethanol solution.

Based on the effective fabrication of the two-component

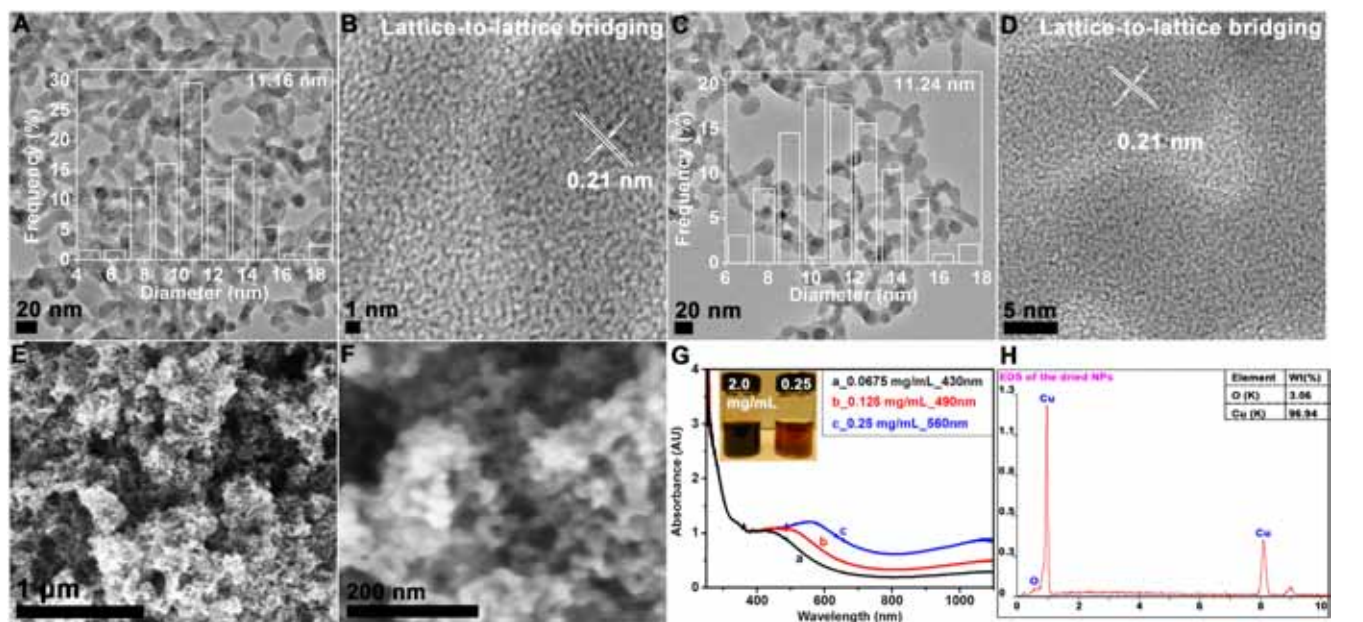


Fig. 2. TEM images of the Cu NPs with the reaction time of (A and B) 2 and (C and D) 4 h, respectively. (E and F) SEM images, (G) UV–vis absorbance spectra, and (H) the corresponding EDS spectrum and element content of the 4 h–resulted Cu NPs. The insets in (A) and (C), and (G) show the size distribution histograms of the corresponding particles and optical photos of the particle solutions, respectively.

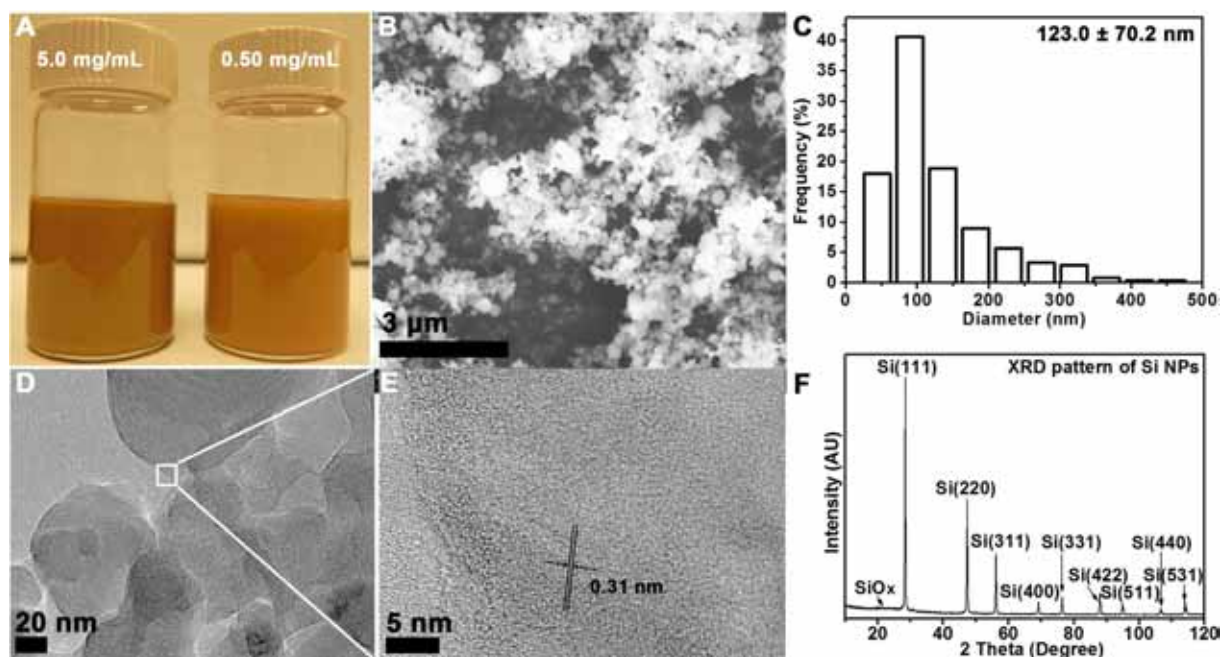


Fig. 3. (A) Optical photographs of (a) 5.0 and (b) 0.50 mg mL⁻¹ Si particle aqueous dispersions. (B) SEM image, (C) size distribution histogram based on the calculation in the SEM image, (D) low- and (E) high-resolution TEM images, and (F) XRD pattern of the Si particles.

nanocomposites by the electrostatic self-assembly process, we were able to fabricate three-component [(PU/Cu-Si)_m(PU/Cu)_n]_N nanocomposites by simply adjusting the solution type and deposition sequence (Fig. 4). All the films were brown yellow (Fig. 7A and B), whether they were deposited on the copper or glass substrates. Due to the high stretchability of PU [31], these free-standing composite films removed from the substrates can be periodically bent without destruction (Fig. 7C). Metallic gloss can be also seen on the surface of the nanocomposite films, so they may show high electro-conductivity, which was previously proved by the SEM images taken without sputtering of gold or carbon (Fig. 7D–I and S3–8). The top surfaces were coarser than the back, due to the vertical growth of the films on the substrate surfaces.

Owing to the difference in the morphology and zeta potential of the Si and Cu particles, some nano-/micro-sized voids generated in the nanocomposites. The small pores may be detrimental to the mechanical properties, however, they would accommodate Si volumetric change by occupying the void space upon lithiation/delithiation. The Si particles were nearly covered by the Cu NP-based ligaments, helpful to increasing the nanocomposite electro-conductivity. In addition, the 90 bilayer PU/Cu-Si nanocomposite film was ~3.5 μm in thickness (Fig. 7H). Although the growth rates of the films assembled on the copper and glass surfaces were different due to change in supporting substrate, both the films showed the same microstructure and color (Figs. 7 and S3–8). TEM further revealed that the Cu NPs formed three-

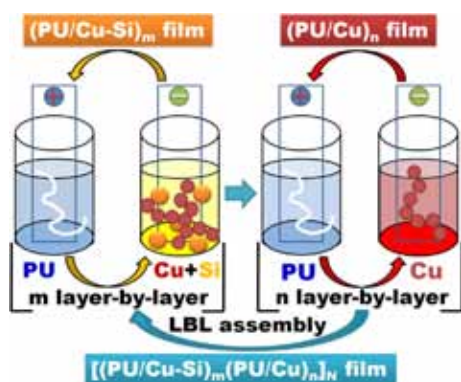


Fig. 4. Schematic description of an improved layer-by-layer (LBL) self-assembly process for flexible nanocomposite films.

dimensional metal networks in the nanocomposites and Si particles were trapped in the PU- and Cu-based networks (Fig. 7J and K), which would impart the films enhanced mechanical robustness and electro-conductivity, and avoid the direct contact of the electrolyte when using the nanocomposites as electrodes in LIBs.

Increasing the electrical conductivity of Si-based films is important to improving the cycle performance for high-rate LIBs. Carbon nanomaterials such as graphene and carbon nanotubes are usually used to prepare carbon/Si (C/Si) composites to improve the conductivity of Si-

based anode materials. In this study, we would verify that the low-cost Cu can also effectively enhance the conductivity of Si-based composite materials. The as-synthesized Cu NPs were inevitably oxidized in water/air, which may have affected the conductivity of the assembled composite films. However, the Cu NPs interconnected to each other to form the chained structure (Fig. 2). Even in the self-assembled nanocomposite films (Figs. 5 and 7 and S3-8), the Cu NPs connected to each other, resulting in the 3D metal conductive net structures. Thus, the nanocomposite films would also exhibit high conductivity (Fig. 8A and S9). The 140 bilayer PU/Cu film displayed a high conductivity of $\sim 106 \text{ S cm}^{-1}$ (Fig. S9). Certainly the $[(\text{PU/Cu-Si})_{12}(\text{PU/Cu})_n]_N$ nanocomposites showed a relatively low conductivity, due to the incorporation of Si particles into the PU/Cu nanocomposite. As thus, the assembly cycle number (n) of (PU/Cu) was increased to enhance the conductivity of the films. When increasing the n from 0 to 6, the conductivity of ~ 126 bilayer films were elevated from 1 to 8 S cm^{-1} (Fig. 8A). This conductive film should afford rapid charge transportation for high-rate LIBs.

The early studies have proven the ultrahigh mechanical strength of the PU-based films [31,45,50]. The superior mechanical tensile property (21.2 MPa and 274.5%) can be achieved by pure PU film prepared by filtrating PU-based aqueous solution (Fig. 8B). When adding Si and Cu nanomaterials into PU films by LBL self-assembly, the mechanical properties of the PU-based nanocomposite films became poor. Exactly, the two- and three-component Cu-based nanocomposite films exhibited moderate ultimate strengths of 11.5 and 8.2 MPa with the corresponding strains of 130.0% and 125.1%, respectively. We also

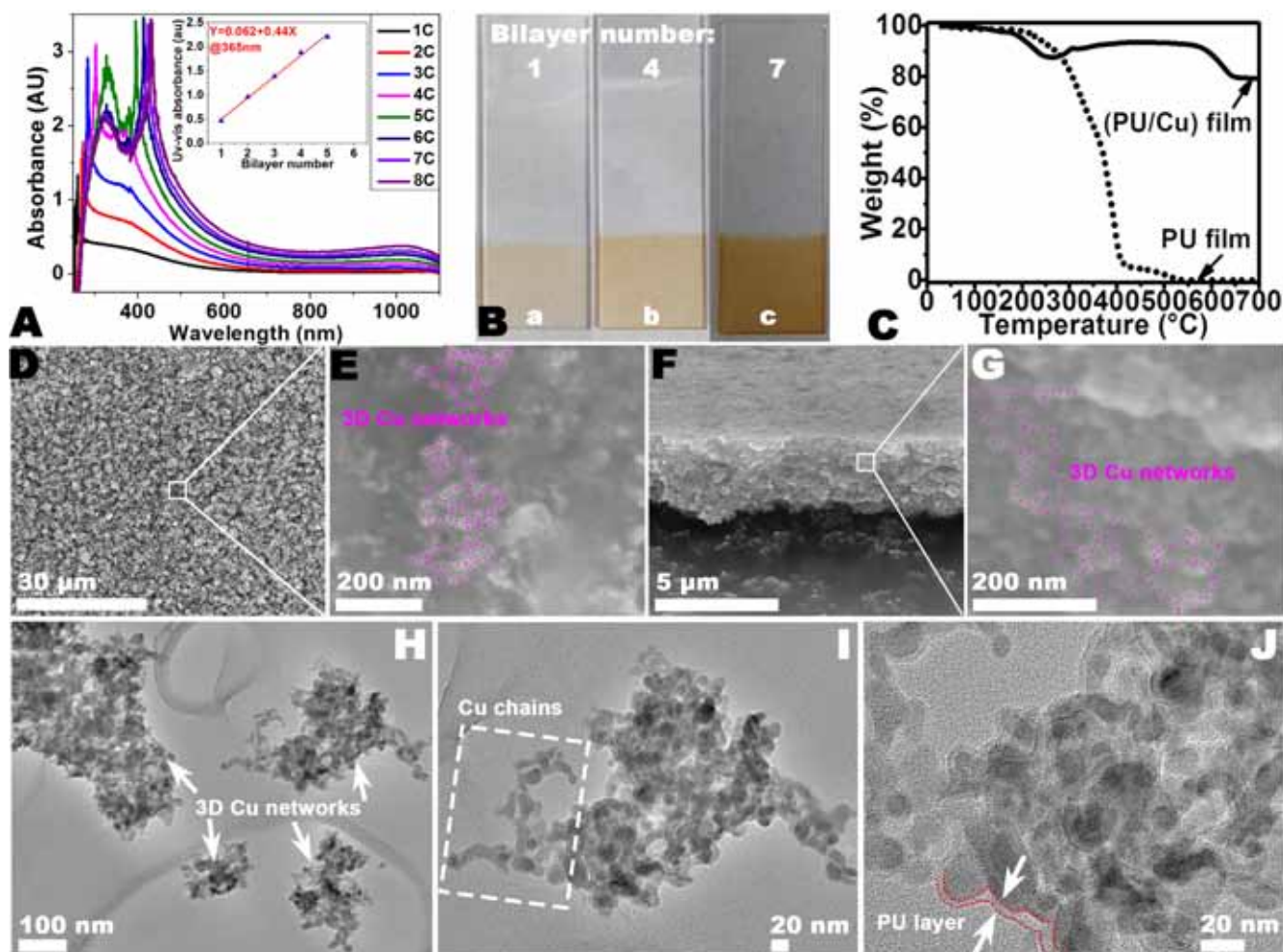


Fig. 5. (A) UV-vis absorbance spectra, (B) optical images, (C) TGA curves, (D and E) surface and (F and G) lateral-section SEM pictures, and (H-J) TEM pictures (after sonication treatment in ethanol for 30 min) of polyurethane/copper composites.

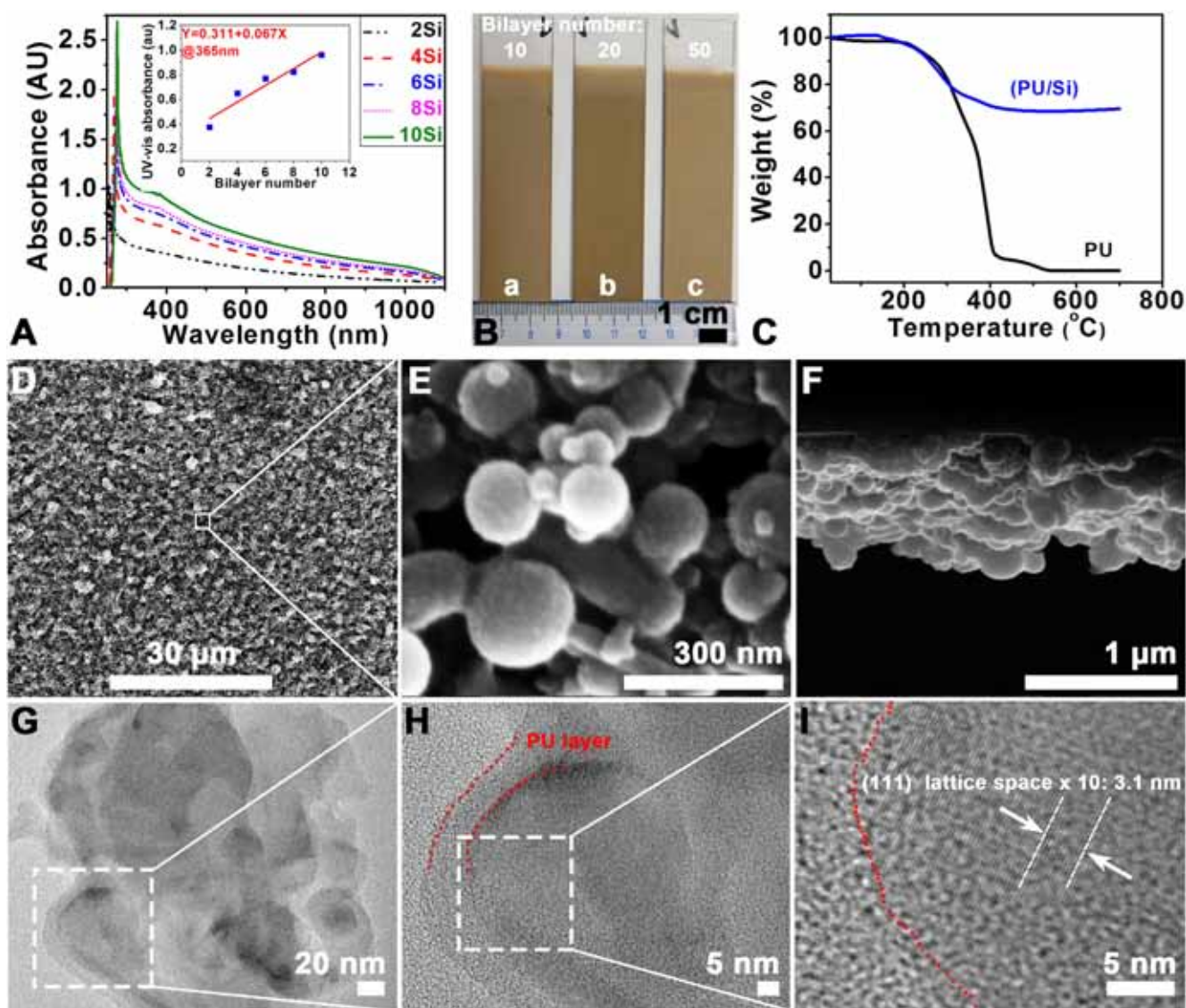


Fig. 6. (A) UV-vis absorbance spectra, (B) optical images, (C) TGA curves, (D and E) surface and (F) lateral-section SEM pictures, and (G–I) TEM pictures (after sonication treatment in ethanol for 30 min) of polyurethane/silicon composites.

fabricated PU/Cu/Si composites by mechanical mixing of the aqueous solutions of the three components and following filtration and desiccation; however, the nanocomposite films easily cracked into pieces (Fig. S10). This further proved the importance of the LBL self-assembly method for preparing high-quality films with nanometer/molecule-level regulation of material structure and inhibition of phase separation and particle aggregation in the solutions. The excellent mechanical properties of the LBL-resulted composite films should enable the toleration of the volumetric change of Si during battery cycling.

3.3. Electrochemical properties of the nanocomposite-based batteries

The coin-type half-cells were fabricated by directly applying the flexible and conductive composite films as anodes for LIB applications. In this work, the specific capacities of the $[(\text{PU/Cu-Si})_m(\text{PU/Cu})]_N$ nanocomposite electrodes were calculated based on the Si contents. The weight ratios of Si in the nanocomposites with the m value of 2, 4 and 6 were detected to be 8.30%, 12.24% and 14.15%, respectively (Fig. S11–14). All the nanocomposite-based cells were periodically charged/discharged at 1.0 C for 300 cycles (Fig. 9A and B). The $[(\text{PU/Cu-Si})_6(\text{PU/Cu})]_N$ nanocomposite-based cells showed a high reversible

capacity of 815 mAh g^{-1} , twice that of the theoretic capacity ($\sim 370 \text{ mAh g}^{-1}$) of the graphite anode. Because of the first three pre-cycles at 0.1 C, the cells displayed a superior first-cycle Coulombic efficiency ($\sim 98.4\%$) at 1.0 C. The cells also showed a specific capacity of 352 mAh g^{-1} after 300 charge-discharge cycles, and the capacity degradation rate was calculated to be only 0.19% for one charge-discharge cycle. Furthermore, $[(\text{PU/Cu-Si})_4(\text{PU/Cu})]_N$ and $[(\text{PU/Cu-Si})_2(\text{PU/Cu})]_N$ nanocomposite-based cells showed the similar capacity degradation rates of 0.18% and 0.17%, respectively, which should be ascribed to high stretchability of the nanocomposites, and the relief of the Si volumetric variation and preservation of copper-formed net structures.

The electrochemical potential profiles of $[(\text{PU/Cu-Si})_2(\text{PU/Cu})]_N$ nanocomposite-based cells at 1.0 C were obtained to disclose the capacity fading behavior (Fig. 9C). The cells exhibited the classical smooth and sloping curves without obvious potential platforms, which were related to the lithiation/delithiation behaviors of amorphous Si that was transformed from the crystalline Si NPs in the pre-cycling instead of capacitance effect (Fig. S15) [51–57]. After 1, 2, 100, 200 and 300 cycles, the cells displayed specific capacities of 1152, 1111, 690, 601 and 574 mAh g^{-1} , respectively. The capacity degradation ratios were 0.40%, 0.13% and 0.04% per C-D cycle for the 1st, 2nd and 3rd

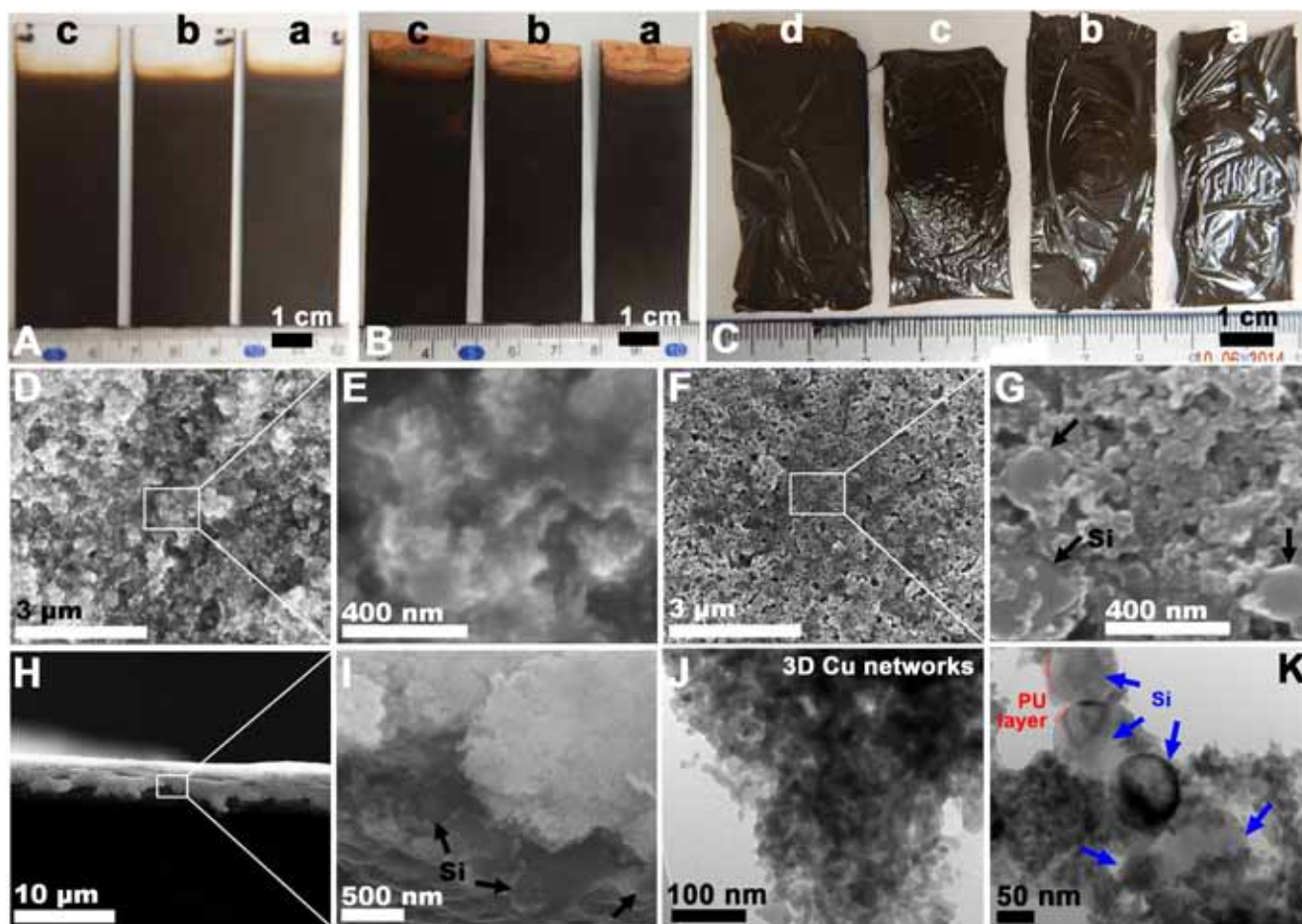


Fig. 7. Optical images of $[(\text{PU}/\text{Cu-Si})_m(\text{PU}/\text{Cu})_n]_N$ nanocomposites grown on (A) glass and (B) copper substrates, and (C) the free-standing films (m : (a) 2, (b) 4, (c) 6 and (d) 1, respectively; N corresponded to 42, 25 and 18 with the n of 1, and to 90 with the n of 0, respectively). SEM pictures of (D and E) top surface, (F and G) bottom surface and (H and I) lateral section, and (J and K) TEM pictures of $(\text{PU}/\text{Cu-Si})_{90}$ film treated by sonication in ethanol solution for 10 and 30 min, respectively.

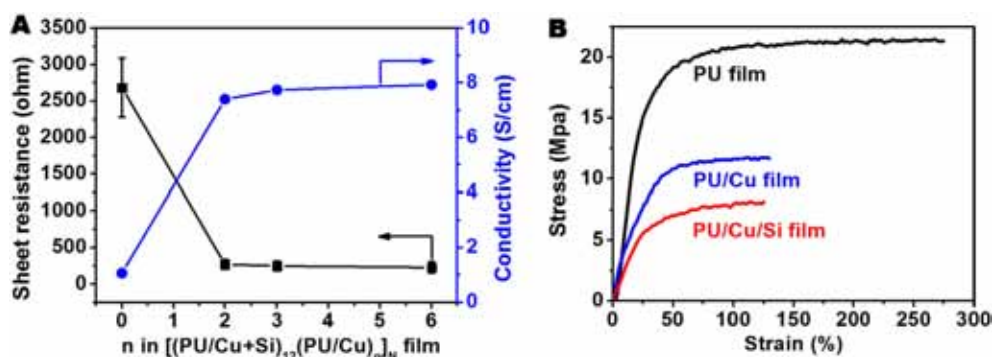


Fig. 8. (A) The dependences of electro-conductivity and resistance on assembly cycle number (n) of (PU/Cu) in $[(\text{PU}/\text{Cu-Si})_{12}(\text{PU}/\text{Cu})_n]_N$ nanocomposites. The entire bilayer numbers defined as $(12 + n) \times N$ were around 126, and the resistances were divided by the thicknesses of the nanocomposite film to obtain the electro-conductivities. (B) Mechanical tensile profiles of free-standing $(\text{PU}/\text{Cu})_{140}$ and $[(\text{PU}/\text{Cu-Si})_2(\text{PU}/\text{Cu})_{110}]_N$ nanocomposite films.

hundred C-D cycles, respectively. The decreasing capacity degradation rate during the electrochemical cycling is beneficial to the practical applications of the film electrodes.

Moreover, the specific capacities of $[(\text{PU}/\text{Cu-Si})_m(\text{PU}/\text{Cu})_n]_N$ nanocomposite-based cells increased greatly with decreasing m value, due to the enhanced conductivity. During the 300 C-D cycles, single and average Coulombic efficiencies of 97.1–101.0% and 99.2–99.8% were obtained for all the film cells, respectively (Fig. 9B). It should be noted that the Coulombic efficiencies and specific capacity of 574 mAh g^{-1} during the 300 high-rate cycles were superior to those in the recent literatures (Table 1) [5,58–64]. We attributed the greatly-improved electrochemical performance to the high electro-conductivity and flexibility of the nanocomposites and the polyurethane layers deposited

on the Si particle surfaces (Figs. 6G-I and 7K), which would alleviate the Si particle expansion/shrinkage upon lithiation/delithiation, prohibit the direct exposure of the Si particles to the electrolyte and suppress the excessive formation of SEI films (Fig. 1B) [40,64].

The rate performance measurements of the three film electrodes (Fig. 9D) disclosed that $[(\text{PU}/\text{Cu-Si})_2(\text{PU}/\text{Cu})_n]_N$ nanocomposite-based cell displayed superior rate capacities than $[(\text{PU}/\text{Cu-Si})_4(\text{PU}/\text{Cu})_n]_N$ and $[(\text{PU}/\text{Cu-Si})_6(\text{PU}/\text{Cu})_n]_N$ nanocomposite-based cells. When increasing the C-D rate from 0.10 to 2.0 C, the nanocomposite electrodes showed 25–30% retention of the original capacities, which was much higher than the slurry-coated electrodes composed of Si, PVDF binder and conductive graphite (2–8%) (Fig. S16). Additionally, when cycled at 0.10 C rate again after the previous 50 cycles, high capacity retentions

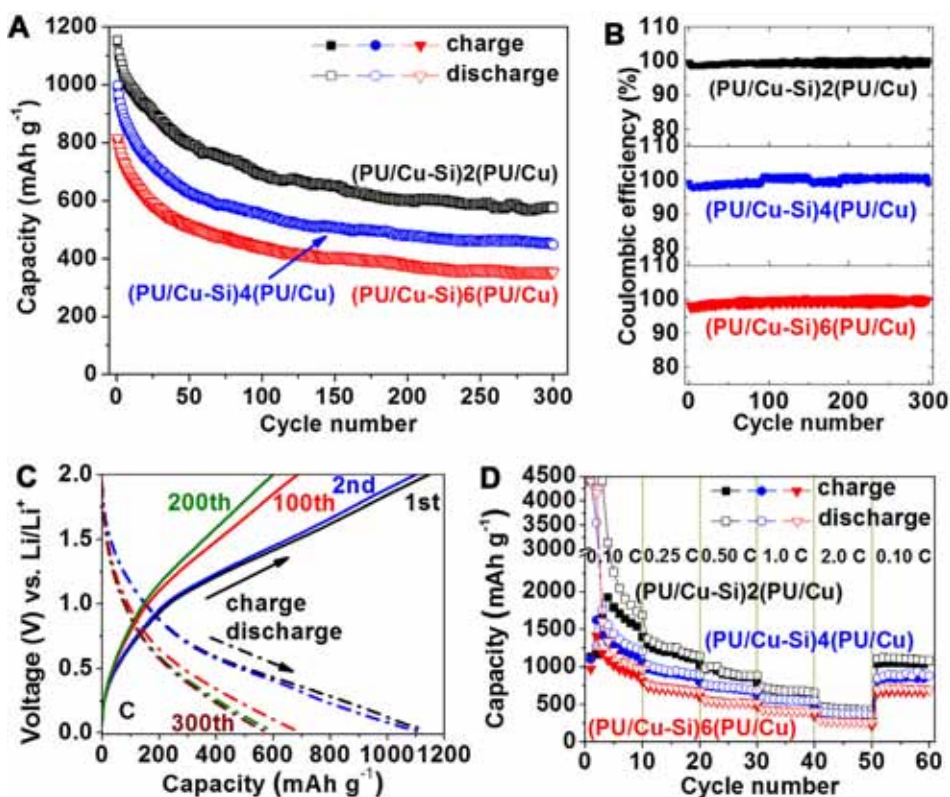


Fig. 9. (A) Cycling performance and (B) Coulombic efficiencies of [(PU/Cu-Si)_m(PU/Cu)]_N nanocomposite-based cells at 1.0 C. (C) Electrochemical potential profiles of (PU/Cu-Si)₂(PU/Cu) electrode at 1st, 2nd, 100th, 200th, and 300th cycle between 0.01 and 2.0 V. (D) Rate performance of the nanocomposite-based cells.

of 72%, 73% and 64% were achieved by the [(PU/Cu-Si)₆(PU/Cu)]_N, [(PU/Cu-Si)₄(PU/Cu)]_N and [(PU/Cu-Si)₂(PU/Cu)]_N nanocomposite-based cells, respectively.

The EIS spectra were further used to investigate the electrochemical process of the nanocomposite-based cells (Fig. 10A and B). According to previous papers [47,69], the circles in high- and medium-frequency regions were attributed to the SEI formation and contact resistance, and charge-transfer impedance at electrolyte/electrode interface, respectively, while the line in the low-frequency area reflected the Li diffusion behavior in the electrodes. An equivalent circuit model was also applied for quantitative analysis of the electrochemical reactions (Fig. 10D) [47,69]. R_f and C_f are the resistance and capacitance regarding to SEI film, respectively. R_e and Z_w are the electrolyte resistance and Warburg impedance, respectively. R_{ct} and C_{dl} are the charge-transfer resistance and double-layer capacitance, respectively. Moreover, the exchange

current densities were calculated by an equation [47,69]: $i_o = (RT)/(nFR_{ct})$, where F , T , n and R represent Faraday constant, absolute temperature, the number of transferred electrons and gas constant, respectively.

No matter being tested for 0 or 300 C-D cycles, the [(PU/Cu-Si)₂(PU/Cu)]_N nanocomposite-based cell had the smallest semicircle diameter (Fig. 10A and B), which indicated that decreasing the assembly number (m) was an effective method for forming denser Cu-based conductive networks in the nanocomposites and facilitating the charge transfer (Fig. 8A). We can also observe that R_{ct} decreased greatly with the decreasing m value (from 6 to 2) in Table 2, because of the decreasing Si content and increasing Cu content in the nanocomposite films. After 300 high-rate cycling at 1 C, R_{ct} increased owing to the huge Si volumetric change and the destruction of the 3D Cu conductive networks. However, R_f increased very slowly during the

Table 1
Cycling performance of reported high-rate (≥ 0.5 C) Si-based anodes.

Anode type	Fabrication route	Capacity (mAh g ⁻¹)	Coulombic efficiency (%)		Cycle	C rate	Ref.
			Single	Average			
Flexible nanocomposite	LBL self-assembly by electrostatic attraction	574	97.1–101.0	99.2–99.8	300	1.0 C	Our
		690	–	–	100		
Silicon/carbon composite	Electrospinning	600	–	–	100	1.0 C	[58]
	Electrospinning and metallothermic reduction	765	~99.5% (280th)	–	280	0.5 C	[59]
Silicon nanolayer-embedded graphite/carbon hybrid	Chemical vapor deposition (CVD)	496	99.5% (100th)	–	100	0.5 C	[60]
Si/edge-activated graphite composite	Ni-catalyzed hydrogenation and CVD	521	~100% (50th)	–	50	0.5 C	[61]
Porous copper supported Si/Ta film	Vapor deposition	700	~100% (200th)	–	200	0.5 C	[62]
Si/graphene film	Vacuum filtering	< 200	–	–	6	1.0 C	[65]
Si@void@graphene nanoparticle	Template method	~1000	–	–	10	0.5 C	[66]
PAN/Si/Ni foam	Plasma enhanced CVD	~700	–	–	10	0.75 C	[67]
Si/carbon/graphene composite	Spray drying	~900	–	–	8	0.5 C	[68]

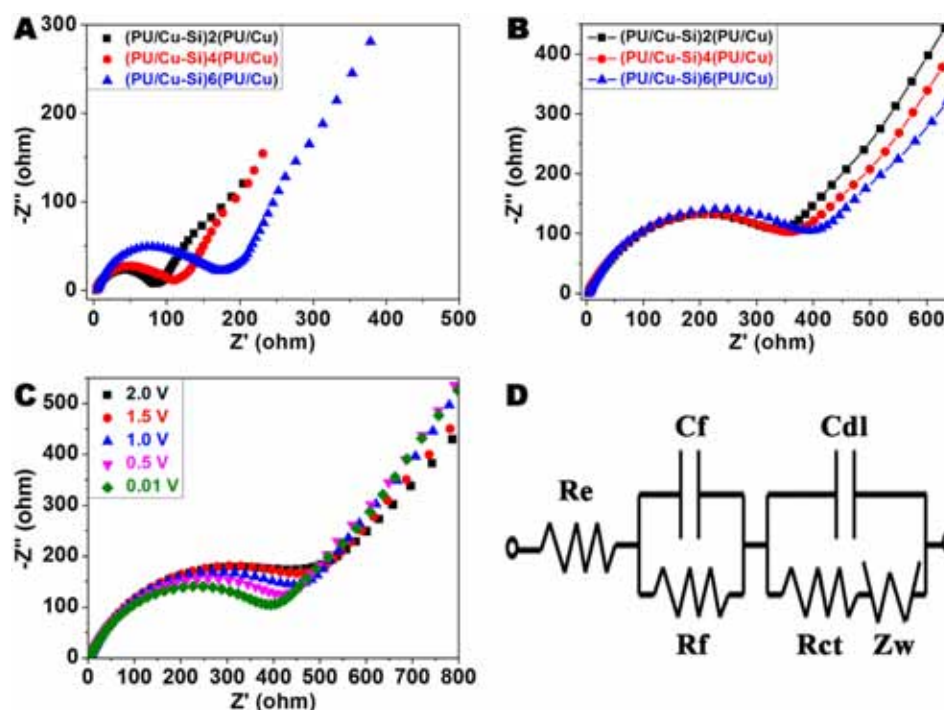


Fig. 10. Impedance spectra of nanocomposite-based cells between 100k and 0.01 Hz (A) before and (B) after the 1.0 C cycling at 1.0 C, and of (C) [(PU/Cu-Si)₆(PU/Cu)]_N film electrode at different potentials. (D) An equivalent circuit model for half-cells.

Table 2
Electrochemical parameters of the film electrodes.

Electrode type	Cycle number	R_f (ohm)	R_{ct} (ohm)	i_0 (A cm ⁻²)
[(PU/Cu-Si) ₂ (PU/Cu)]	0	18.8	53.3	4.80×10^{-4}
	300	20.7	196.1	1.31×10^{-4}
[(PU/Cu-Si) ₄ (PU/Cu)]	0	25.8	62.8	4.08×10^{-4}
	300	27.9	220.4	1.16×10^{-4}
[(PU/Cu-Si) ₆ (PU/Cu)]	0	27.4	112.4	2.28×10^{-4}
	300	30.3	244.5	1.05×10^{-4}

whole cycling, which should be attributed to the entire encapsulation of the Si particles by the cationic PU matrices (Figs. 6 and 7). Previous study also proved that PU can effectively absorb on the surfaces of active electrode particles and current collectors by the opposite charge attraction interaction and prohibit the electrolyte attack [40].

Furthermore, we investigated the impedance changes of the film electrode at various potentials (Fig. 10C). The R_{ct} decreased from 269.3 Ω at 2.0 V to 265.9 Ω at 1.5 V, 259.0 Ω at 1.0 V, 249.8 Ω at 0.5 V, and 244.8 Ω at 0.01 V, indicating that the charge transfer became easier (Table 3). Because Li_xSi exhibited higher conductivity than pure Si, so when the potential decreased, more Li_xSi generated on the Si particle surfaces, and the R_{ct} decreased and the charge transfer was facilitated [70,71]. For bare Si particle-based electrode, too thick SEI layer on Si surface will hinder the charge transfer (Fig. 1A), so the R_{ct} and R_f should increase when the lithiation was nearly finished [72]. However, the R_{ct} and R_f of the nanocomposite film electrode remained decreasing, and

Table 3
Electrochemical parameters of [(PU/Cu-Si)₆(PU/Cu)]_N film electrode.

Potential (V)	R_f (ohm)	R_{ct} (ohm)	i_0 (A cm ⁻²)
2.0	32.6	269.3	9.51×10^{-5}
1.5	32.3	265.9	9.63×10^{-5}
1.0	30.4	259.0	9.88×10^{-5}
0.5	28.7	249.8	1.02×10^{-4}
0.01	30.4	244.8	1.05×10^{-4}

the i_0 increased from 9.51×10^{-5} A cm⁻² at 2.0 V to 1.05×10^{-4} A cm⁻² at the final potential of 0.01 V (Table 3), which should be ascribed to the enhanced electrical conductivity of the nanocomposite electrode, and the effective suppression of SEI formation by the PU matrix (Fig. 1B) [70].

SEM and TEM were furtherly used to detect the morphological change of the nanocomposite electrodes after the 1.0 C electrochemical cycling for 300 cycles. As for the [(PU/Cu-Si)₆(PU/Cu)]_N nanocomposite, a few cracks and pores generated (Fig. 11A and B), because of the large volumetric variation of the Si particles. When decreasing the m value to 4, the number of cracks and pores also decreased (Fig. 11D and E), owing to the increasing Cu networks and decreasing Si mass in the nanocomposite. However, no obvious cracks and pores were observed in the [(PU/Cu-Si)₂(PU/Cu)]_N nanocomposite (Fig. 11G and H), because of the effective alleviation of the Si volumetric change by the flexible nanocomposite. Together with the TEM images (taken after the sonication treatment of the nanocomposites), we also found that the Si particles were fully encapsulated with the 3D Cu networks (Fig. 11J and K), which could promote the electron transfer in the nanocomposites. Moreover, the Si particles were still entirely covered by the flexible and ion-conducting PU (Fig. 11L), which can greatly relieve the Si volumetric change-induced internal stress by the PU shape change and meanwhile block the direct exposure to the electrolyte and suppress the SEI formation. These results were consistent with the analyses of the battery cycling and electrochemical impedances (Figs. 9 and 10).

4. Conclusions

LBL self-assembly technology was used for fabricating multi-functional nanocomposite films with property integrity of the three building blocks—Si, Cu and PU through their strong electrostatic attractions. The 1D chains and 3D networks of Cu in the nanocomposites furtherly facilitated the electron transfer. The free-standing PU/Cu/Si nanocomposite films had high mechanical flexibility and electro-conductivity, which would greatly tolerate the Si volumetric variation upon lithiation/delithiation and maintain the charge transport. The stretchable and ion-conducting PU matrix in the films can also prevent

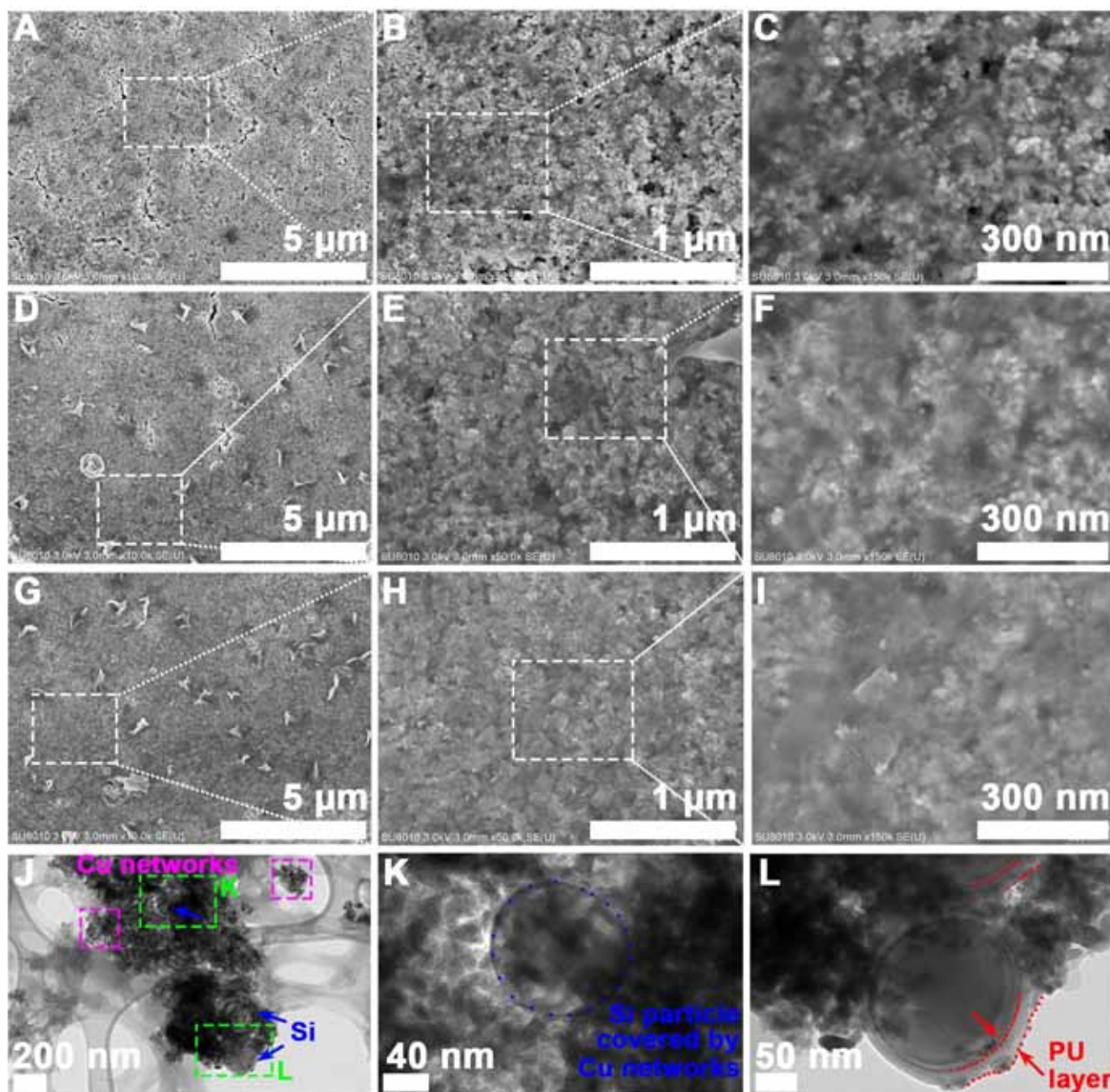


Fig. 11. SEM pictures of the $[(\text{PU}/\text{Cu-Si})_m(\text{PU}/\text{Cu})]_N$ nanocomposites with m value of (A–C) 6, (D–F) 4 and (G–I) 2 as battery electrodes after the 1.0 C cycling, respectively. (J) Low- and (K and L) high-resolution TEM pictures of the nanocomposite with m value of 2 after the 1.0 C cycling (after sonication treatment in ethanol).

the SEI generation on the Si particles. Therefore, the film electrodes exhibited superior capacity and Coulombic efficiencies, which are comparable to the values of the recently-developed Si-based electrodes. Compared with the traditional mixing method for composites, the LBL self-assembly technology can not only avoid the phase separation and particle aggregation in the NP solutions but also realize the multifunctional films. We can envision that the LBL self-assembly method can be also utilized for simple and effective fabrication of various multifunctional composite films for wide applications including flexible batteries and supercapacitors.

Conflicts of interest

There are no conflicts of interest to declare.

Acknowledgment

We are grateful for the funding supports: Natural Science Foundation of Beijing Municipality (L172036), Science and Technology Beijing 100 Leading Talent Training Project, Par-Eu Scholars Program, Beijing Municipal Science and Technology Project (Z161100002616039), Joint Funds of the Equipment Pre-Research and Ministry of Education (6141A020225), China Postdoctoral Science Foundation (2018M631419), NCEPU “Double First-Class” Graduate Talent Cultivation Program, and the Fundamental Research Funds for the Central Universities (2016JQ01, 2017ZZD02).

Appendix A. Supplementary material

Supplementary data to this article can be found online at <https://doi.org/10.1016/j.apsusc.2019.01.075>.

References

- [1] T.W. Kwon, J.W. Choi, A. Coskun, The emerging era of supramolecular polymeric binders in silicon anodes, *Chem. Soc. Rev.* 47 (2018) 2145–2164, <https://doi.org/10.1039/c7cs00858a>.
- [2] K. Feng, M. Li, W. Liu, A.G. Kashkooli, X. Xiao, M. Cai, Z. Chen, Silicon-based anodes for lithium-ion batteries: from fundamentals to practical applications, *Small* 14 (2018) 1702737, <https://doi.org/10.1002/smll.201702737>.
- [3] W. Luo, X. Chen, Y. Xia, M. Chen, L. Wang, Q. Wang, W. Li, J. Yang, Surface and interface engineering of silicon-based anode materials for lithium-ion batteries, *Adv. Energy Mater.* 7 (2017) 1701083, <https://doi.org/10.1002/aenm.201701083>.
- [4] A. Franco Gonzalez, N.-H. Yang, R.-S. Liu, Silicon anode design for lithium-ion batteries: progress and perspectives, *J. Phys. Chem. C* 121 (2017) 27775–27787, <https://doi.org/10.1021/acs.jpcc.7b07793>.
- [5] J. Yang, Y. Wang, W. Li, L. Wang, Y. Fan, W. Jiang, W. Luo, Y. Wang, B. Kong, C. Selomulya, H.K. Liu, S.X. Dou, D. Zhao, Amorphous TiO₂ shells: a vital elastic buffering layer on silicon nanoparticles for high-performance and safe lithium storage, *Adv. Mater.* 29 (2017) 1700523, <https://doi.org/10.1002/adma.201700523>.
- [6] H. Kim, M. Seo, M.H. Park, J. Cho, A critical size of silicon nano-anodes for lithium rechargeable batteries, *Angew. Chem. Int. Ed.* 49 (2010) 2146–2149, <https://doi.org/10.1002/anie.200906287>.
- [7] M.T. McDowell, S.W. Lee, I. Ryu, H. Wu, W.D. Nix, J.W. Choi, Y. Cui, Novel size and surface oxide effects in silicon nanowires as lithium battery anodes, *Nano Lett.* 11 (2011) 4018–4025, <https://doi.org/10.1021/nl202630n>.
- [8] M.-H. Park, M.G. Kim, J. Joo, K. Kim, J. Kim, S. Ahn, Y. Cui, J. Cho, Silicon nanotube battery anodes, *Nano Lett.* 9 (2009) 3844–3847, <https://doi.org/10.1021/nl902058c>.
- [9] L. Liu, J. Lyu, T. Li, T. Zhao, Well-constructed silicon-based materials as high-performance lithium-ion battery anodes, *Nanoscale* 8 (2016) 701–722, <https://doi.org/10.1039/C5NR06278K>.
- [10] K. Fu, L. Xue, O. Yildiz, S. Li, H. Lee, Y. Li, G. Xu, L. Zhou, P.D. Bradford, X. Zhang, Effect of CVD carbon coatings on Si@CNF composite as anode for lithium-ion batteries, *Nano Energy* 2 (2013) 976–986, <https://doi.org/10.1016/j.nanoen.2013.03.019>.
- [11] M. Sadeghipari, A. Mashayekhi, S. Mohajerzadeh, Novel approach for improving the performance of Si-based anodes in lithium-ion batteries, *Nanotechnology* 29 (2018) 055403, <https://doi.org/10.1088/1361-6528/aaa0e7>.
- [12] N. Liu, H. Wu, M.T. McDowell, Y. Yao, C. Wang, Y. Cui, A yolk-shell design for stabilized and scalable Li-ion battery alloy anodes, *Nano Lett.* 12 (2012) 3315–3321, <https://doi.org/10.1021/nl3014814>.
- [13] Y. Han, J. Zou, Z. Li, W. Wang, Y. Jie, J. Ma, B. Tang, Q. Zhang, X. Cao, S. Xu, Z.L. Wang, Si@void@C nanofibers fabricated using a self-powered electrospinning system for lithium-ion batteries, *ACS Nano* 12 (2018) 4835–4843, <https://doi.org/10.1021/acsnano.8b01558>.
- [14] H. Liu, Y. Zou, L. Huang, H. Yin, C. Xi, X. Chen, H. Shentu, C. Li, J. Zhang, C. Lv, M. Fan, Enhanced electrochemical performance of sandwich-structured polyaniline-wrapped silicon oxide/carbon nanotubes for lithium-ion batteries, *Appl. Surf. Sci.* 442 (2018) 204–212, <https://doi.org/10.1016/j.apsusc.2018.02.023>.
- [15] M. Ge, X. Fang, J. Rong, C. Zhou, Review of porous silicon preparation and its application for lithium-ion battery anodes, *Nanotechnology* 24 (2013) 422001, <https://doi.org/10.1088/0957-4484/24/42/422001>.
- [16] L. Liu, J. Lyu, T. Zhao, T. Li, L. Liu, J. Lyu, T. Zhao, T. Li, Preparations and properties of porous copper materials for lithium-ion battery applications, *Chem. Eng. Commun.* 6445 (2016) 707–713, <https://doi.org/10.1080/00986445.2015.1104504>.
- [17] Z. Zhang, Z.L. Wang, X. Lu, Multishelled Si@Cu microparticles supported on 3D Cu current collectors for stable and binder-free anodes of lithium-ion batteries, *ACS Nano* 12 (2018) 3587–3599, <https://doi.org/10.1021/acsnano.8b00703>.
- [18] S.R. Gowda, V. Pushparaj, S. Herle, G. Girishkumar, J.G. Gordon, H. Gullapalli, X. Zhan, P.M. Ajayan, A.L.M. Reddy, Three-dimensionally engineered porous silicon electrodes for Li ion batteries, *Nano Lett.* 12 (2012) 6060–6065, <https://doi.org/10.1021/nl302114j>.
- [19] L.H. Liu, J. Lyu, T.K. Zhao, T.H. Li, N. Polytechnical, A. Arbor, Roles of preparation conditions in the morphological evolution of electrodeposited copper, *Dig. J. Nanomater. Biostructures* 12 (2017) 1021–1030.
- [20] L. Liu, M. Li, J. Lyu, T. Zhao, T. Li, Facile and green preparation of three-dimensionally nanoporous copper films by low-current electrical field-induced assembly of copper nanoparticles for lithium-ion battery applications, *J. Mater. Eng. Perform.* 27 (2018) 4680–4692, <https://doi.org/10.1007/s11665-018-3583-4>.
- [21] L.-F. Cui, L. Hu, J.W. Choi, Y. Cui, Light-weight free-standing carbon nanotube-silicon films for anodes of lithium ion batteries, *ACS Nano* 4 (2010) 3671–3678, <https://doi.org/10.1021/nn100619m>.
- [22] B. Wang, X. Li, B. Luo, Y. Jia, L. Zhi, One-dimensional/two-dimensional hybridization for self-supported binder-free silicon-based lithium ion battery anodes, *Nanoscale* 5 (2013) 1470, <https://doi.org/10.1039/c3nr33288h>.
- [23] M. Dirican, O. Yildiz, Y. Lu, X. Fang, H. Jiang, H. Kizil, X. Zhang, Flexible binder-free silicon/silica/carbon nanofiber composites as anode for lithium-ion batteries, *Electrochim. Acta* 169 (2015) 52–60, <https://doi.org/10.1016/j.electacta.2015.04.035>.
- [24] M. Zhou, X. Li, B. Wang, Y. Zhang, J. Ning, Z. Xiao, X. Zhang, Y. Chang, L. Zhi, High-performance silicon battery anodes enabled by engineering graphene assemblies, *Nano Lett.* 15 (2015) 6222–6228, <https://doi.org/10.1021/acs.nanolett.5b02697>.
- [25] L. Liu, F. Xie, J. Lyu, T. Zhao, T. Li, B.G. Choi, Tin-based anode materials with well-designed architectures for next-generation lithium-ion batteries, *J. Power Sources* 321 (2016) 11–35, <https://doi.org/10.1016/j.jpowsour.2016.04.105>.
- [26] X. Tang, G. Wen, Y. Song, Stable silicon/3D porous N-doped graphene composite for lithium-ion battery anodes with self-assembly, *Appl. Surf. Sci.* 436 (2018) 398–404, <https://doi.org/10.1016/j.apsusc.2017.12.068>.
- [27] B.S. Shim, P. Podsiadlo, D.G. Lilly, A. Agarwal, J. Lee, Z. Tang, S. Ho, P. Ingle, D. Paterson, W. Lu, N.A. Kotov, Nanostructured thin films made by dewetting method of layer-by-layer assembly, *Nano Lett.* 7 (2007) 3266–3273, <https://doi.org/10.1021/nl071245d>.
- [28] A. Mamedov, J. Ostrander, F. Aliev, N.A. Kotov, Stratified assemblies of magnetite nanoparticles and montmorillonite prepared by the layer-by-layer assembly, *Langmuir* 16 (2000) 3941–3949, <https://doi.org/10.1021/la990957j>.
- [29] J. Zhu, H. Zhang, N.A. Kotov, Thermodynamic and structural insights into nanocomposites engineering by comparing two materials assembly techniques for graphene, *ACS Nano* 7 (2013) 4818–4829, <https://doi.org/10.1021/nm400972t>.
- [30] T. Lee, S.H. Min, M. Gu, Y.K. Jung, W. Lee, J.U. Lee, D.G. Seong, B.-S. Kim, Layer-by-layer assembly for graphene-based multilayer nanocomposites: synthesis and applications, *Chem. Mater.* 27 (2015) 3785–3796, <https://doi.org/10.1021/acs.chemmater.5b00491>.
- [31] Y. Kim, J. Zhu, B. Yeom, M. Di Prima, X. Su, J.-G. Kim, S.J. Yoo, C. Uher, N.A. Kotov, Stretchable nanoparticle conductors with self-organized conductive pathways, *Nature* 500 (2013) 59–63, <https://doi.org/10.1038/nature12401>.
- [32] L. Zhou, Q. Cao, B. Jing, X. Wang, X. Tang, N. Wu, Study of a novel porous gel polymer electrolyte based on thermoplastic polyurethane/poly(vinylidene fluoride-co-hexafluoropropylene) by electrospinning technique, *J. Power Sources* 263 (2014) 118–124, <https://doi.org/10.1016/j.jpowsour.2014.03.140>.
- [33] L. Liu, X. Wu, T. Li, Novel polymer electrolytes based on cationic polyurethane with different alkyl chain length, *J. Power Sources* 249 (2014) 397–404, <https://doi.org/10.1016/j.jpowsour.2013.10.116>.
- [34] L. Liu, L. Chu, B. Jiang, M. Li, Li_{1.4}Al_{0.4}Ti_{1.6}(PO₄)₃ nanoparticle-reinforced solid polymer electrolytes for all-solid-state lithium batteries, *Solid State Ionics* 331 (2019) 89–95, <https://doi.org/10.1016/j.ssi.2019.01.007>.
- [35] S.R. Mustapa, M.M. Aung, A. Ahmad, A. Mansor, L. TianKhook, Preparation and characterization of Jatropha oil-based polyurethane as non-aqueous solid polymer electrolyte for electrochemical devices, *Electrochim. Acta* 222 (2016) 293–302, <https://doi.org/10.1016/j.electacta.2016.10.173>.
- [36] X. Tang, Q. Cao, X. Wang, X. Peng, J. Zeng, Study of the effect of a novel high-performance gel polymer electrolyte based on thermoplastic polyurethane/poly(vinylidene fluoride)/polystyrene and formed using an electrospinning technique, *RSC Adv.* 5 (2015) 58655–58662, <https://doi.org/10.1039/C5RA08493H>.
- [37] X. Zou, Q. Lu, Y. Zhong, K. Liao, W. Zhou, Z. Shao, Flexible, flame-resistant, and dendrite-impermeable gel-polymer electrolyte for Li–O₂/air batteries workable under hurdle conditions, *Small* 14 (2018) 1–10, <https://doi.org/10.1002/smll.201801798>.
- [38] N. Ren, Y. Song, C. Tao, B. Cong, Q. Cheng, Y. Huang, G. Xu, J. Bao, Effect of the soft and hard segment composition on the properties of waterborne polyurethane-based solid polymer electrolyte for lithium ion batteries, *J. Solid State Electrochem.* 22 (2018) 1109–1121, <https://doi.org/10.1007/s10008-017-3855-1>.
- [39] B. Cong, Y. Song, N. Ren, G. Xie, C. Tao, Y. Huang, G. Xu, J. Bao, Polyethylene glycol-based waterborne polyurethane as solid polymer electrolyte for all-solid-state lithium ion batteries, *Mater. Des.* 142 (2018) 221–228, <https://doi.org/10.1016/j.matdes.2018.01.039>.
- [40] N. Loeffler, T. Kopel, G.-T. Kim, S. Passerini, Polyurethane binder for aqueous processing of Li-ion battery electrodes, *J. Electrochem. Soc.* 162 (2015) A2692–A2698, <https://doi.org/10.1149/2.0641514jes>.
- [41] G. Zainab, X. Wang, J. Yu, Y. Zhai, A. Ahmed Babar, K. Xiao, B. Ding, Electrospun polyacrylonitrile/polyurethane composite nanofibrous separator with electrochemical performance for high power lithium ion batteries, *Mater. Chem. Phys.* 182 (2016) 308–314, <https://doi.org/10.1016/j.matchemphys.2016.07.037>.
- [42] X. Liu, K. Song, C. Lu, Y. Huang, X. Duan, S. Li, Y. Ding, Electrospun PU@GO separators for advanced lithium ion batteries, *J. Memb. Sci.* 555 (2018) 1–6, <https://doi.org/10.1016/j.memsci.2018.03.027>.
- [43] Y. Wang, T. Asefa, Poly(allylamine)-stabilized colloidal copper nanoparticles: synthesis, morphology, and their surface-enhanced Raman scattering properties, *Langmuir* 26 (2010) 7469–7474, <https://doi.org/10.1021/la904199f>.
- [44] S. Chowdhury, V.R. Bhethanabotla, R. Sen, Effect of Ag–Cu alloy nanoparticle composition on luminescence enhancement/quenching, *J. Phys. Chem. C* 113 (2009) 13016–13022, <https://doi.org/10.1021/jp900294z>.
- [45] P. Podsiadlo, M. Qin, M. Cuddihy, J. Zhu, K. Critchley, E. Kheng, A.K. Kaushik, Y. Qi, H.-S. Kim, S.-T. Noh, E.M. Arruda, A.M. Waas, N.A. Kotov, Highly ductile multilayered films by layer-by-layer assembly of oppositely charged polyurethanes for biomedical applications, *Langmuir* 25 (2009) 14093–14099, <https://doi.org/10.1021/la9021323>.
- [46] L.H. Liu, J. Lyu, T.H. Li, T.K. Zhao, Facile and green synthesis of stable aqueous dispersions of narrowly distributed copper nanoparticles, *Dig. J. Nanomater. Biostructures* 10 (2015) 1303–1310.
- [47] L. Liu, B.G. Choi, S.O. Tung, T. Hu, Y. Liu, T. Li, T. Zhao, N.A. Kotov, Low-current field-assisted assembly of copper nanoparticles for current collectors, *Faraday Discuss.* 181 (2015) 383–401, <https://doi.org/10.1039/C4FD00263F>.
- [48] C. Wu, B.P. Mosher, T. Zeng, One-step green route to narrowly dispersed copper

- nanocrystals, *J. Nanoparticle Res.* 8 (2006) 965–969, <https://doi.org/10.1007/s11051-005-9065-2>.
- [49] P. Kanninen, C. Johans, J. Merta, K. Kontturi, Influence of ligand structure on the stability and oxidation of copper nanoparticles, *J. Colloid Interface Sci.* 318 (2008) 88–95, <https://doi.org/10.1016/j.jcis.2007.09.069>.
- [50] A.K. Kaushik, P. Podsiadlo, M. Qin, C.M. Shaw, A.M. Waas, N.A. Kotov, E.M. Arruda, The role of nanoparticle layer separation in the finite deformation response of layered polyurethane-clay nanocomposites, *Macromolecules* 42 (2009) 6588–6595, <https://doi.org/10.1021/ma901048g>.
- [51] S. Guo, H. Li, H. Bai, Z. Tao, J. Chen, Ti/Si/Ti sandwich-like thin film as the anode of lithium-ion batteries, *J. Power Sources* 248 (2014) 1141–1148, <https://doi.org/10.1016/j.jpowsour.2013.09.138>.
- [52] C. Yu, X. Li, T. Ma, J. Rong, R. Zhang, J. Shaffer, Y. An, Q. Liu, B. Wei, H. Jiang, Silicon thin films as anodes for high-performance lithium-ion batteries with effective stress relaxation, *Adv. Energy Mater.* 2 (2012) 68–73, <https://doi.org/10.1002/aenm.201100634>.
- [53] H. Li, F. Cheng, Z. Zhu, H. Bai, Z. Tao, J. Chen, Preparation and electrochemical performance of copper foam-supported amorphous silicon thin films for rechargeable lithium-ion batteries, *J. Alloys Compd.* 509 (2011) 2919–2923, <https://doi.org/10.1016/j.jallcom.2010.11.156>.
- [54] A. Gohier, B. Laïk, K.-H. Kim, J.-L. Maurice, J.-P. Pereira-Ramos, C.S. Cojocaru, P.T. Van, High-rate capability silicon decorated vertically aligned carbon nanotubes for Li-ion batteries, *Adv. Mater.* 24 (2012) 2592–2597, <https://doi.org/10.1002/adma.201104923>.
- [55] B. Wang, X. Li, B. Luo, X. Zhang, Y. Shang, A. Cao, L. Zhi, Intertwined network of Si/C nanocables and carbon nanotubes as lithium-ion battery anodes, *ACS Appl. Mater. Interfaces* 5 (2013) 6467–6472, <https://doi.org/10.1021/am402022n>.
- [56] T. Shen, X. Xia, D. Xie, Z. Yao, Y. Zhong, J. Zhan, D. Wang, J. Wu, X. Wang, J. Tu, Encapsulating silicon nanoparticles into mesoporous carbon forming pomegranate-structured microspheres as a high-performance anode for lithium ion batteries, *J. Mater. Chem. A.* 5 (2017) 11197–11203, <https://doi.org/10.1039/C7TA03294C>.
- [57] X. Ma, G. Hou, Q. Ai, L. Zhang, P. Si, J. Feng, L. Ci, A heart-coronary arteries structure of carbon nanofibers/graphene/silicon composite anode for high performance lithium ion batteries, *Sci. Rep.* 7 (2017) 9642, <https://doi.org/10.1038/s41598-017-09658-4>.
- [58] Y. Liu, K. Huang, Y. Fan, Q. Zhang, F. Sun, T. Gao, Z. Wang, J. Zhong, Binder-free Si nanoparticles@carbon nanofiber fabric as energy storage material, *Electrochim. Acta.* 102 (2013) 246–251, <https://doi.org/10.1016/j.electacta.2013.04.021>.
- [59] J. Ryu, S. Choi, T. Bok, S. Park, Nanotubular structured Si-based multicomponent anodes for high-performance lithium-ion batteries with controllable pore size via coaxial electro-spinning, *Nanoscale* 7 (2015) 6126–6135, <https://doi.org/10.1039/C5NR00224A>.
- [60] M. Ko, S. Chae, J. Ma, N. Kim, H.W. Lee, Y. Cui, J. Cho, Scalable synthesis of silicon-nanolayer-embedded graphite for high-energy lithium-ion batteries, *Nat. Energy* 1 (2016) 1–8, <https://doi.org/10.1038/nenergy.2016.113>.
- [61] N. Kim, S. Chae, J. Ma, M. Ko, J. Cho, Fast-charging high-energy lithium-ion batteries via implantation of amorphous silicon nanolayer in edge-plane activated graphite anodes, *Nat. Commun.* 8 (2017) 1–10, <https://doi.org/10.1038/s41467-017-00973-y>.
- [62] M. Haro, V. Singh, S. Steinhauer, E. Toulkeridou, P. Grammatikopoulos, M. Sowwan, Nanoscale heterogeneity of multilayered Si anodes with embedded nanoparticle scaffolds for Li-ion batteries, *Adv. Sci.* 4 (2017) 1700180, <https://doi.org/10.1002/advs.201700180>.
- [63] D. Vrankovic, M. Graczyk-Zajac, C. Kalcher, J. Rohrer, M. Becker, C. Stabler, G. Trykowski, K. Albe, R. Riedel, Highly porous silicon embedded in a ceramic matrix: a stable high-capacity electrode for Li-ion batteries, *ACS Nano* 11 (2017) 11409–11416, <https://doi.org/10.1021/acsnano.7b06031>.
- [64] E. Greco, G. Nava, R. Fathi, F. Fumagalli, A.E. Del Rio-Castillo, A. Ansaldo, S. Monaco, F. Bonaccorso, V. Pellegrini, F. Di Fonzo, Few-layer graphene improves silicon performance in Li-ion battery anodes, *J. Mater. Chem. A.* 5 (2017) 19306–19315, <https://doi.org/10.1039/C7TA05395A>.
- [65] H. Zhang, S. Jing, Y. Hu, H. Jiang, C. Li, A flexible freestanding Si/rGO hybrid film anode for stable Li-ion batteries, *J. Power Sources* 307 (2016) 214–219, <https://doi.org/10.1016/j.jpowsour.2015.12.107>.
- [66] X. Ding, X.X. Liu, Y. Huang, X. Zhang, Q. Zhao, X. Xiang, G. Li, P. He, Z. Wen, J. Li, Y. Huang, Enhanced electrochemical performance promoted by monolayer graphene and void space in silicon composite anode materials, *Nano Energy* 27 (2016) 647–657, <https://doi.org/10.1016/j.nanoen.2016.07.031>.
- [67] W. Bao, J. Wang, S. Chen, W. Li, Y. Su, F. Wu, G. Tan, J. Lu, A three-dimensional hierarchical structure of cyclized-PAN/Si/Ni for mechanically stable silicon anodes, *J. Mater. Chem. A.* 5 (2017) 24667–24676, <https://doi.org/10.1039/c7ta08744f>.
- [68] Q. Pan, P. Zuo, S. Lou, T. Mu, C. Du, X. Cheng, Y. Ma, Y. Gao, G. Yin, Micro-sized spherical silicon@carbon@graphene prepared by spray drying as anode material for lithium-ion batteries, *J. Alloys Compd.* 723 (2017) 434–440, <https://doi.org/10.1016/j.jallcom.2017.06.217>.
- [69] P. Guo, H. Song, X. Chen, Electrochemical performance of graphene nanosheets as anode material for lithium-ion batteries, *Electrochem. Commun.* 11 (2009) 1320–1324, <https://doi.org/10.1016/j.elecom.2009.04.036>.
- [70] F. Wang, S. Xu, S. Zhu, H. Peng, R. Huang, L. Wang, X. Xie, P.K. Chu, Ni-coated Si microchannel plate electrodes in three-dimensional lithium-ion battery anodes, *Electrochim. Acta* 87 (2013) 250–255, <https://doi.org/10.1016/j.electacta.2012.09.122>.
- [71] H. Wu, G. Yu, L. Pan, N. Liu, M.T. McDowell, Z. Bao, Y. Cui, Stable Li-ion battery anodes by in-situ polymerization of conducting hydrogel to conformally coat silicon nanoparticles, *Nat. Commun.* 4 (2013) 1943, <https://doi.org/10.1038/ncomms2941>.
- [72] W.-R. Liu, J.-H. Wang, H.-C. Wu, D.-T. Shieh, M.-H. Yang, N.-L. Wu, Electrochemical characterizations on Si and C-coated Si particle electrodes for lithium-ion batteries, *J. Electrochem. Soc.* 152 (2005) A1719, <https://doi.org/10.1149/1.1954967>.